Universität
Zürich^UZH

Master Thesis

X-SNSPDs based on high temperature superconductor

Physik-Institut
Faculty of Science
University of Zurich

April 20, 2018

Student: Andreas Meier

Group: Prof. Dr. Andreas Schilling

Advisor: Prof. Dr. Andreas Schilling

Co-Advisor: Dr. Qiang Wang

Abstract

As recently developing single photon detectors, Superconducting Nanowire Single Photon Detectors (SNSPDs) have shown wide applications in quantum optics, quantum communications and bio-science, due to their outstanding performances, e.g. highspeed, low darkcounts and a very broad optical detection spectra.

Based on the previous study of SNSPDs for X-ray detection (X-SNSPDs), we extend the normal superconductors (Nb, NbN, NbTiN, etc.) to the high temperature superconductors (e.g. cuprate superconductors). We concentrate our main efforts on YBaCuO (YBCO) superconductor films and we also initially explore the more promising BiSrCaCuO superconductor films.

In order to fabricate YBCO-based X-SNSPDs we first characterize the critical temperature and critical current of the YBCO thick films (150 nm), and then we fabricate the thick films into nano structures including single bridges and meandering wires. However, no evident X-ray single photon response is observed. The main reason could be the larger thickness, leading to a low sensitivity to single photons. We then try thinner YBCO films (40 nm and 20 nm). After fabrication the thinner films suffer strongly from degradation, due to the oxygen loss in YBCO films.

Finally we tried BiSrCaCuO films, which are more robust in nano fabrication compared to YBCO films. We have shown that, for BSCCO micro scale bridges a proper annealing process makes its critical temperature back to the original value (~ 95 K), indicating a very promising potential for the X-SNSPDs experiment in the next step.

Table of Contents

1 Introduction

1.1 Superconductivity

Superconductivity was discovered in 1911 by H. Kamerlingh Onnes [1], just 3 years after he had first liquefied helium, which gave him the refrigeration technique required to reach temperatures of a few Kelvin. What Kamerlingh Onnes observed was that the electrical resistance of various metals such as mercury (Figure 1), lead and tin decreased to an unmeasurable low value in a small temperature range below a critical temperature T_c. Later, permanent current-experiments suggested that the resistance is indeed zero or at least very close to zero [2].
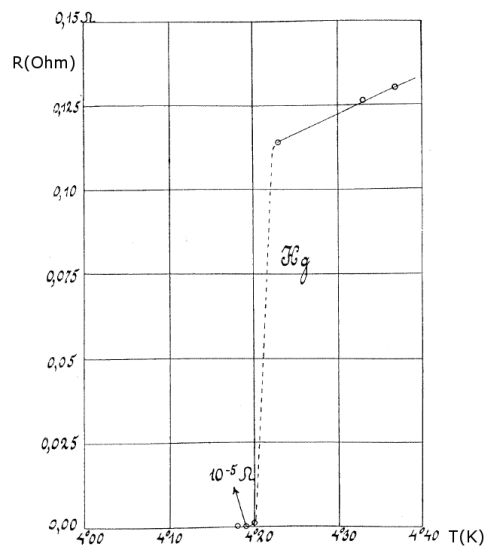

Figure 1: Historic plot of resistance (Ohm) versus temperature (K) for mercury from 1911 experiment shows the superconducting transition at $4.20\,\mathrm{K}$ [3].

The next hallmark to be discovered was perfect diamagnetism, found in 1933 by W. Meissner and R. Ochsenfeld. They found that not only is a magnetic field preventet from entering a superconductor, as might appear to be explained by perfect conductivity, but also that a field in an originally normal sample is expelled as it is cooled through T_c (Fig. 2). The existence of such a reversible Meissner effect implies that superconductivity will be destroyed by a critical magnetic field H_c. The description of this effect was possible by the development of the phenomenological London theory [2].
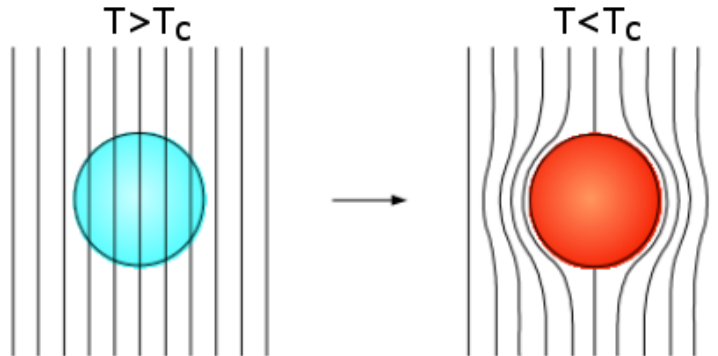
Figure 2: Schematic diagram of exclusion of magnetic flux from interior of massive superconductor. A normal state sphere (green) is full of magnetic flux, while as the temperature goes below T_c, the fluxes are expelled (red). Indicating diamagnetic property of the massive superconductor [4].

In 1950 the Ginzburg-Landau (GL) theory of superconductivity was presented by V. L. Ginzburg and L. D. Landau. They introduced a complex pseudowavefunction φ as an order parameter within Landau's general theory of second-order phase transitions. This φ describes the superconducting electrons, and the local density of superconducting electrons was given by

$$n_s = |\varphi(x)|^2. \tag{1}$$

Two of the most important conclusions are drawn from GL theory. On the one hand a length scale is introduced over which the order parameter φ and therefore the density of superconducting charge carriers n_s can vary, and the scale is called the Ginzburg-Landau coherence length ξ_{GL}. On the other hand, GL theory confirmed the results of the London theory which claims that an external magnetic field can penetrate a superconductor up to the characteristic length λ_L, the London penetration depth. In the framework of Ginzburg and Landau, this parameter is called the Ginzburg-Landau penetration depth λ_{GL}. The ratio of the two characteristic lengths defines the GL parameter

$$\kappa = \frac{\lambda_{GL}}{\xi_{GL}}. \tag{2}$$

The superconductors are categorized into 2 types: $\kappa < \frac{1}{\sqrt{2}}$, type I superconductor with "classical" behaviour described above, and $\kappa > \frac{1}{\sqrt{2}}$ type II superconductor. Instead of discontinuous breakdown of superconductivity in a first-order transition at H_c, there was a continuous increase in flux penetration starting at a lower critical field H_{c1} and reaching $B = H$ at an upper critical field H_{c2}.

In 1957, more than four decades after the discovery of superconductivity, J. Bardeen, L. N. Cooper and J. R. Schrieffer were able to show that, due to interactions with the lattice ions, electrons can feel an attractive force and form a

kind of bound state, so-called BCS theory [5]. The theory was able to explain all observed phenomena up to now. In this theory the characteristic BCS coherence length ξ_0 is defined as the length scale over which the two electrons of a Cooper pair interact.

According to the BCS theory a minimum energy $E_g = 2\Delta(T)$ is required to break a pair, creating two quasi-particle excitations. This $\Delta(T)$ was predicted to increase from zero at T_c to a limiting value

$$E_g = 2\Delta(0) = 3.528kT_c \tag{3}$$

for $T \ll T_c$. Not only did this result agree with the measured energy gap, but the predicted absorption edge above $\hbar\omega_g = E_g$ was also confirmed by the experiments.

In 1986 J. G. Bednorz and K. A. Mueller discovered high-temperature superconductivity in layered materials (BaLaCuO) dominated by copper oxide planes. Materials of this sort have subsequently been discovered with T_c well over $100\,\text{K}$. This has opened the way to a broader range of practical applications than for the classic superconductors because cooling by liquid helium is not required. It is clear that a two-electron pairing is involved, but the nature of the pairing remains controversial.

M. K. Wu et al. [6] found that another copper oxide $YBa_2Cu_3O_7$ (YBCO) is superconducting with a critical temperature of $93\,\text{K}$, which was the first superconductor found to have a critical temperature above the boiling point of nitrogen at $77\,\text{K}$.
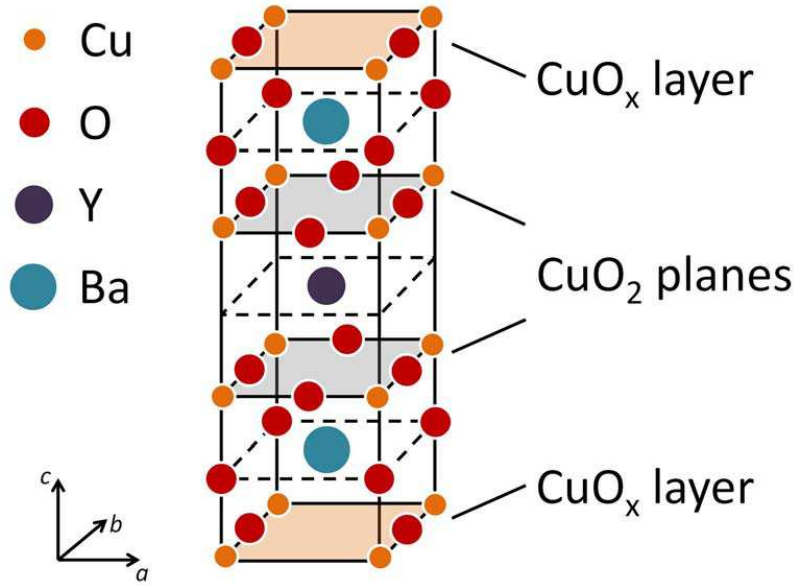
Figure 3: Schematic of the crystal lattice of $YBa_2Cu_3O_{7-x}$ [7] shows the structure with the CuO_2-planes, BaO-planes and CuO_x-layers (b-axis oriented chains).

The perovskite-like crystalline lattice has a characteristic layered structure (Fig. 3). The two copper oxide planes which are separated by an yttrium atom are characteristic of the YBCO unit cell followed by the barium oxide planes. The unit cell is enclosed on both sides by the b-axis-oriented copper oxide chains. With reduced oxygen content more and more oxygen vacancies appear in the chains. The critical temperature decrease with decreasing oxygen content after an initial increase and a maximum of the critical temperature appears at a level of $x \approx 0.1$ [8].

Due to the crystal structure YBCO is a highly anisotropic material. The superconducting length scales show similar anisotropy in both penetration depth ($\lambda_{ab} \approx 150 \, \text{nm}$, $\lambda_c \approx 800 \, \text{nm}$) and coherence length, ($\xi_{ab} \approx 2 \, \text{nm}$, $\xi_c \approx 0.4 \, \text{nm}$). Although the coherence length in the a-b plane is 5 times greater than along the c-axis it is quite small compared to classical superconductors such as Nb ($\xi \approx 40 \, \text{nm}$) [9]. A disadvantage of YBCO is the surface degradation due to decrease in oxygen concentration [10].

H. Maeda et al. [11] reported another superconducting material $BiSrCaCu_2O_x$ with a higher T_c than YBCO. A series of $Bi_2Sr_2Ca_{n-1}Cu_nO_{2n+4+y}$compounds exists in this material family. The best known are the compounds with $n = 1-3$. The crystal structure of $Bi_2Sr_2CaCu_2O_{8+y}$ is shown in Fig. 4.
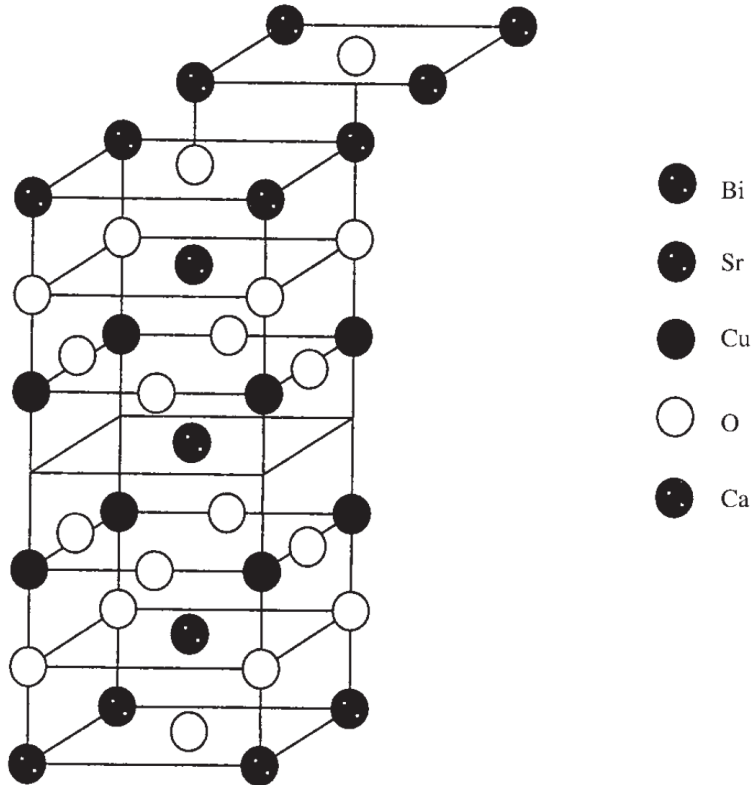
Figure 4: Schematic of the crystal lattice of $Bi_2Sr_2CaCu_2O_{8+y}$ (Bi2212) [12].

The Bi2212 phase has a pseudo-tetragonal structure, with lattice parameters $a \approx b \approx 5.4\,Å$ and $c \approx 30.8\,Å$, which is also anisotropic. The superconducting length scale shows different anisotropy: in penetration depth ($\lambda_{ab} \approx 21\,\mu m$, $\lambda_c \approx 100\,\mu m$) the anisotropy is lower than in coherence length ($\xi_{ab} \approx 19\,Å$, $\xi_c \approx 0.45\,Å$) [12]. Compared to the YBCO films BSCCO films are more robust against oxygen leak and nano fabrication.

1.2 Superconducting Nanowire Single Photon Detector (SN-SPD)

The superconducting state can be destroyed by incident radiation at different wavelengths (especially optical) [13]. The advent of thin superconductor films, nano-fabrication techniques and laser sources allowed for the first superconducting radiation detectors and bolometers for infrared millimeter waves as first demonstrated in Ref. [14].

In 2001 Gol'tsman *et al.* demonstrated a new superconducting device concept for single photon detection, based on NbN nanowires [15]. This type of device, called superconducting single-photon detector (SSPD) or Superconducting Nanowire Single-Photon Detector (SNSPD), is single-photon sensitive on a broad wavelength band (infrared to X-ray, or meV to keV). A typical SNSPD con-

sists of a few nm thin film of a superconducting material such as NbN or WSi, which are fabricated into a meandering wire geometry. The nano fabrication process contains the following steps: a superconducting thin film with a typical thickness of one coherence length is deposited on a substrate. After the fabrication of contact pad (Ti/Au), a meander structure on the film is patterned via electron beam lithography (EBL) and reactive ion etching (RIE). More complex structure like cavities or optical coating are also integrated for better optical absorption efficiency [16].

With a bias current sufficiently close to the critical current of the superconductor meander, the energy of one or several photons can be enough to trigger a local transition to the resistive state. The energy of the absorbed photon is distributed through an avalanche-like process, creating a nonequilibrium population of quasiparticles. This quasiparticle population then disrupts the supercurrent flow, resulting eventually in a detection event.

The simplest model of photon detection in the SNSPDs is the hard normal core model. In this model, when a photon is absorbed by the nanowire a small resistive hotspot is created. The supercurrent is forced to flow along the periphery of the hotspot. Since the nanowires are narrow, the local current density around the hotspot increases, exceeding the superconducting critical current density. This in turn leads to the formation of a resistive barrier across the width of the nanowire. Joule heating aids the growth of resistive region along the axis of the nanowire until the current flow is blocked and the bias current is shunted by the external circuit. This allows the resistive region to subside and the wire becomes fully superconducting again and the bias current through the nanowire returns to the original value [17]. The hot spot model applied well to the very thin nanowire while photon-detection models involving magnetic flux are also put forward to quantitatively understand the SNSPDs. In such models, the amount and distribution of superconducting electrons are changed and redistributed due to the photon absorption, and therefore the barrier potential for the vortex is decreased accordingly. When the vortex can overcome the barrier and move across the wire, the heat dissipation can destroy the superconducting state and trigger the detector [18, 19].

Due to the recovery time of several ns, broad detection spectra and low dark counts there are a lot of applications for SNSPDs as quantum optic, quantum communications and the bio-sciences [20].

Several impressive research results have been published during the past years such as the reported 93 % system detection efficiency based on an optical cavity [21], the timing jitter down to 18 ps [22], and the realization of a 64-pixel SNSPD array [23]. Also new superconducting materials (MgB_2, MoSi, MoGe, etc. [24, 25]) are explored for single photon detection.

1.3 SNSPD for X-ray (X-SNSPD)

In principle, any particle with energy larger than 2Δ of the SNSPD can be detected. A natural extension of applications of SNSPD is photon detection at X-ray regime, which can be used for single molecular, virus or cell CT and X-ray imaging [26].

In 2012, it was shown by K. Inderbitzin et al. [27] that the detection of soft X-ray photons ($\sim 10\,\text{keV}$) with a Nb SNSPD is possible. Compared to the SNSPDs based on a thin superconductor film ($\sim 4\,\text{nm}$) for visible photon detection, the X-SNSPDs for X-ray were made out of a Nb film with a thickness of $100\,\text{nm}$ for higher absorption. With a small bias current of approximately $5.5\,\%$ of the critical current the X-SNSPDs were already able to detect X-ray photons, and no dark count was recorded for $5\,\text{h}$ measurement due to the thick film and the low operation bias current.

In 2013 K. Inderbitzin et al. [28] fabricated a $250\,\text{nm}$ wide TaN X-SNSPD with T_c of $6.7\,\text{K}$ and a detection efficiency of $1.4\,\%$ at a photon energy of $5.9\,\text{keV}$. A significant energy-resolution capability was demonstrated.

Recently Zhang *et al.* [26] reported a X-SNSPD based on $W_{0.8}Si_{0.2}$ wire ($100\,\text{nm}$ thick, $150\,\text{nm}$ wide) with a T_c of $4.8\,\text{K}$ and a detection efficiency of $7.5\,\%$. This detector showed a saturated count rate dependence on bias current at all temperatures up to T_c, indicating that the optimal quantum efficiency can always be reached. Moreover, during the measurement, no dark count is observed even at $99\,\%\ I_c$ and at a temperature close to T_c.

1.4 High Temperature Superconductor (HTS) based X-SNSPDs

The X-SNSPDs introduced above are mostly based on low temperature superconductors. Such detectors can only be operated in a liquid He environment ($\sim 4\,\text{K}$). This critical condition severely limits the applications of X-SNSPD. A promising solution is to explore the high temperature superconductor (HTS) for X-SNSPD fabrication.

We first investigated the YBCO material since YBCO-based micro devices have been extensively investigated and the corresponding fabrication techniques can be used straightforwardly. For visible and infrared photon detection ultra-thin nanowires have allready been processed in $YBa_2Cu_3O_{7-x}$ thin films [29] but single-photon sensitivity has not been demonstrated. The failure of photon-detection applications for YBCO could be due to the low energy of the visible/infrared photons. Therefore we focus on photon-detection in the regime of X-ray, and the main task is to explore T_c, I_c, degradation of YBCO films and narrow wire structures. We hope to find proper parameters (thickness, wire width and length) that can make the YBCO-based X-SNSPD suitable for X-ray detection.

The thesis is organized in the following way: In Chapter 2 the equipment is introduced, including a 70 K Cryostat and a 2 K PPMS. Chapter 3 shows the characterisations of YBCO thin films and nano structures, and also the initial results based on BSCCO are presented. Finally the thesis is concluded in Chapter 4.

2   Equipment

2.1   X-ray sources

Two different X-ray sources are used:

- a radioactive Fe-55 isotope source (activity of 3.7 GBq) emitting X-ray photons of 5.9 eV, as a well-defined reference for calibrating other X-ray sources.

- a tungsten-target X-ray tube (Source 1 X-Ray) with a maximum acceleration voltage of approximately 80 kV and a maximum current of 2 mA.

The old X-ray tube (Oxford Instruments) used before broke during earlier measurements and it has been replaced by the new X-ray tube (Source 1 X-Ray). After installing the new X-ray tube we tried to compare the irradiation power and spectrum of the new tube with the existing data of the old one.

To perform such measurements we adopted a commercial X-ray detector, (Si-PIN X-ray photon counter XPIN-BT by Moxtek) and we use the radioactive Fe-55 isotope source as a calibration reference. In the measurement, the new X-ray tube is installed close to the window of the Cryostat sample chamber, and the commercial detector is fixed at the position where the sample (e.g. X-SNSPD) would be. With manual alignment the whole configuration of the setup allows a homogeneous irradiation of the commercial detector by both sources.

Figure 5 shows the emission spectra of the new, Source 1 X-ray tube (Fig. 5a) and the old, Oxford Instruments X-ray tube (Fig. 5b). Compared to the spectrum of the Oxford tube with 2 typical characteristic peaks, Source 1 tube shows a broad, or Bremsstrahlung behaviour, and at higher currents (e.g. 1.5 mA) the spectrum contains photons with too large energy in respect to the corresponding driven voltage. For example, the red curve in Fig. 5a shows contributions of photons beyond 30 keV while the driven voltage is 30 kV. The explanation for these photons is either double counts (two photons are detected as one) or the unstable voltage source (e.g. ripples in high voltage).

Despite the non-ideal spectrum for the new tube, the total amount of emitted photons (per second) is comparable to the old tube with the same settings of driven voltage and current. With such conditions, we can perform the X-ray detection measurements for the HTS X-SNSPDs.
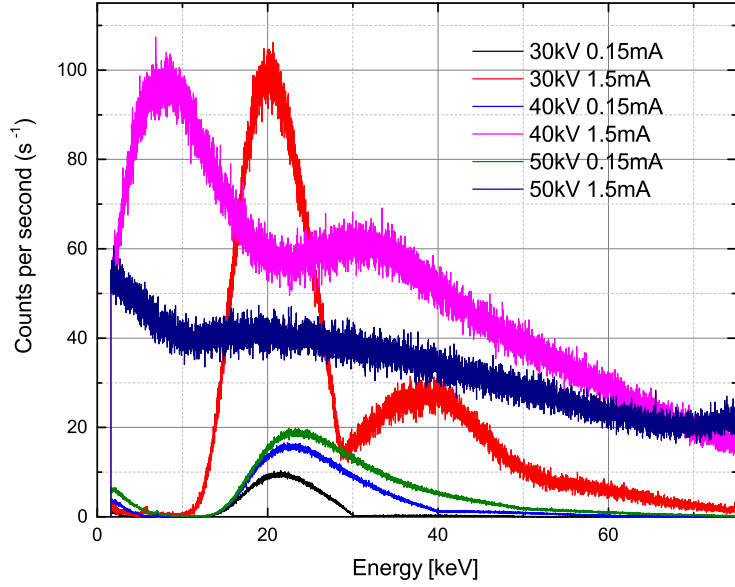
(a)
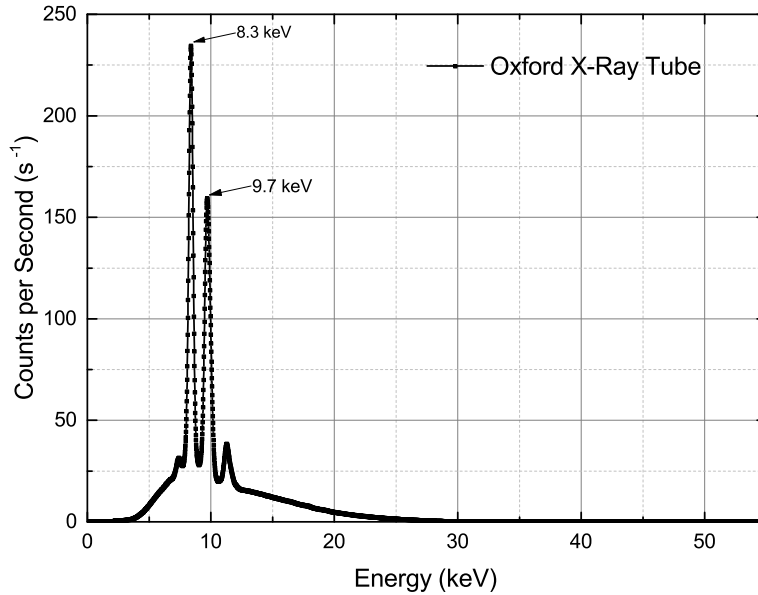
(b)

Figure 5: (a) Emission spectra of the new X-ray tube (Source 1 X-Ray) with different driven current and voltage combinations. With a lower current (0.15 mA), the shape is comparable to the Bremsstrahlung. With a higher current (1.5 mA), the emission spectra change to an unexpected shape. The increased photons with low energy come from radiation of the surrounding materials in the tube excited by the high energy photons. The photon with energy beyond the driven voltage may be due to the unstable voltage source (e.g. ripples in high voltage). (b) Emission spectrum of the old X-ray tube (Oxford Instruments) with an acceleration voltage of 30 kV and a current of approximately 0.005 mA. Well-defined X-ray emission lines of the tungsten target around 8.3 keV and 9.7 keV are indicated.

11

2.2 Cryostat

The detection performance of X-SNSPDs is measured in a *Janis* He-3 bath cryostat with a low temperature range (2 K - 20 K) and a high temperature range (60 K - 80 K). Fig. 6 shows a schematic drawing of the cryostat, where the most important parts for operation are labelled. The He reservoir is enclosed by vacuum which is achieved by a two-step pumping process (turbo-pump and rotary vane pump) and reaches around 10×10^{-5} mbar before transferring liquid helium. The entire wall of the tank acts as a cryogenic pump when it is filled with liquid helium and the vacuum decreases to around 10×10^{-8} mbar. The He reservoir is shielded by a LN_2 bath to reduce black body radiation. The LN_2 is again insulated by vacuum against room temperature. The heat-shields at the bottom of the cryostat are thermally coupled to the respective reservoir. There are two optical openings on two sides of the sample space which allows the sample to be exposed (i.e X-SNSPDs) to X-rays. The optical windows can be closed either by aluminium, quartz glass or polyimide. More details of the cooling principle are explained in Ref. [30]. The detector signal is transmitted to an amplifier at room temperature before being fed into a 3.5 GHz digital oscilloscope (Tektronix, DPO7354). The bias current is applied through the same coaxial cable as the signal and both are separated through a bias tee.

Before the measurements we renewed most of the cables and supplemented the system with a new heater at the sample holder. Therefore we are able to operate with a temperature PID loop (Lake Shore Model 340 Cryogenic Temperature Controller) to stabilize the sample temperature. Different thermometers are used to observe the experiments, two silicon temperature sensors to determine the temperature of the charcoal and the 1 K-pot, a rubidium oxide sensor for the He-3-pot and a Cernox sensor on the sample holder for the temperature of the sample.
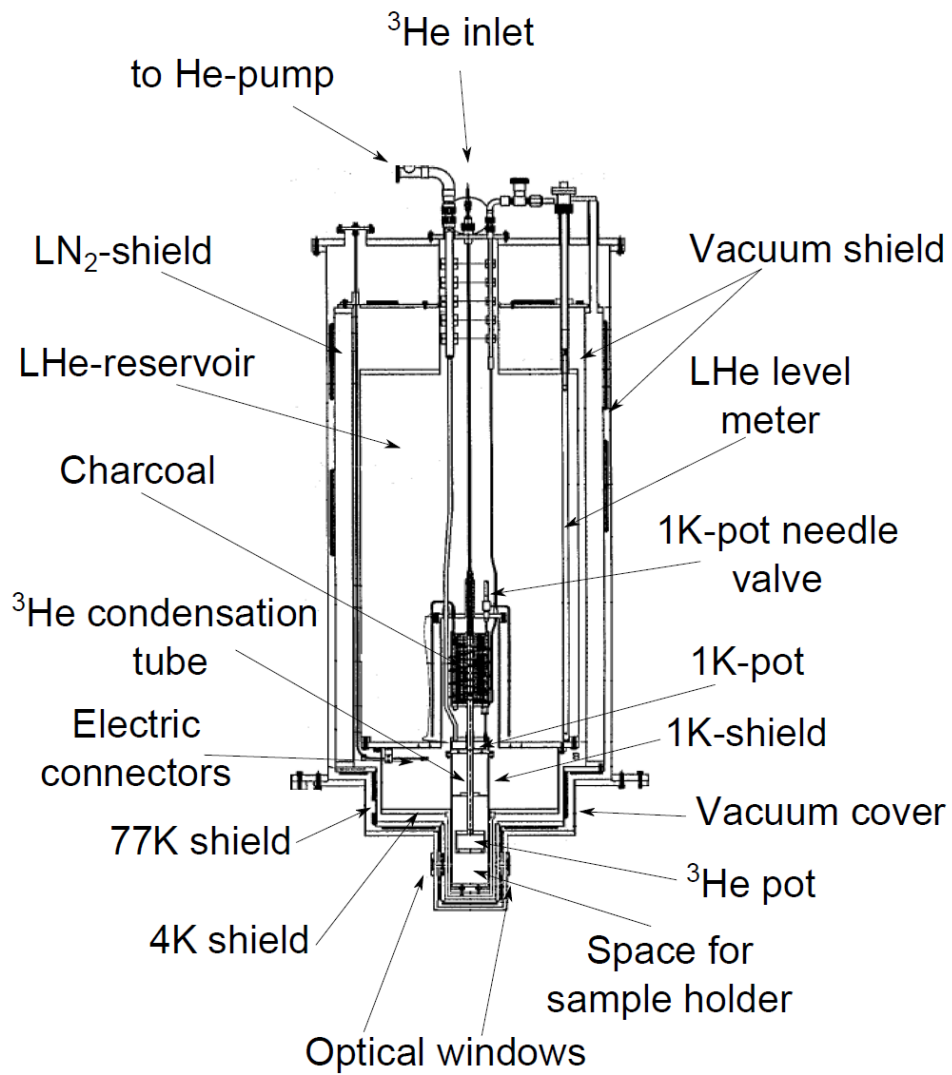
Figure 6: Drawing of the He-3 cryostat [30].

2.3 PPMS

For the film characterisation (in the range of 2 K - 300 K) a physical property measurement system (PPMS) from *Quantum Design* is used. All of the resistivity measurements and several of the I_c measurements were carried out with this system.

2.4 Nano-Processing

The samples of X-SNSPDs (see Fig. 7) are produced in FIRST-lab at ETH. The production process [16] is divided into two parts:

- Outer contact pad: the gold electrodes were produced with the lift-off process. The main process steps are as follows:

  1. Cleaning sample (H_2O and acetone)
  2. Spincoating photoresist AZ5214E
  3. Bake 60 s at 92 °C
  4. Optical lithography
  5. Bake 160 s at 117 °C
  6. Developing 160 s with MF319
  7. H_2O flush
  8. Evaporation 100 nm Cr, 10 nm Ti and 190 nm Au
  9. Lift-off pipette removing with acetone at 50 °C

- Structure: the structure was formed by wet-etching with diluted H_3PO_4. The main process steps are as follows:

  1. Cleaning sample (H_2O and acetone)
  2. Spincoating HSQ
  3. Electron Beam Lithography
  4. Developing 160 s with MFCD26
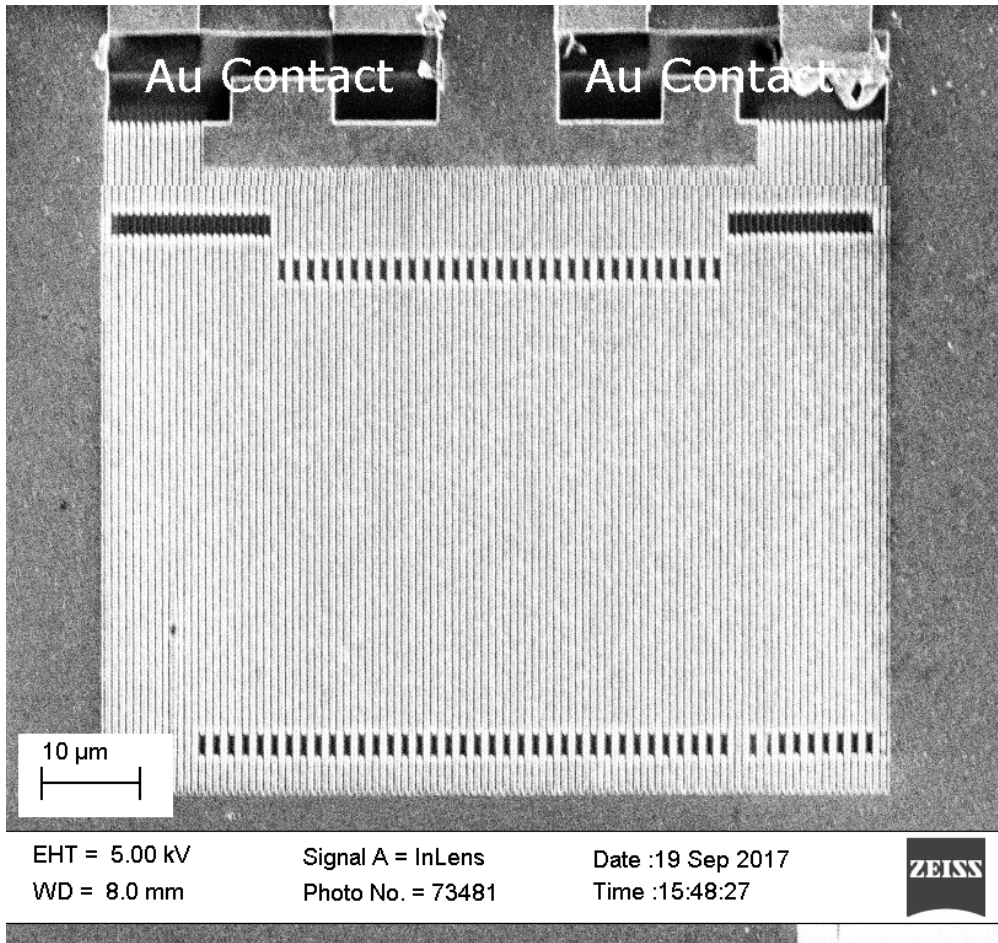 5. Etching with 0.1 % H_3PO_4
  6. Distilled H_2O flush

Figure 7: SEM image of the YBCO-meander fabricated in FIRST-Lab.

3 Results

The YBCO films are deposited via magnetron sputtering on $0.5\,\mathrm{mm}$ thick sapphire substrate by Ceraco. In the lab the films are stored in a dry vacuum box.

3.1   150 nm thick YBCO-films

The first measurements were done with the $150\,\mathrm{nm}$ thick YBCO film. Due to the ceramic properties of YBCO, it is hard to use Reactive Ion Beam Etching to etch YBCO film into meandering wire structure. As a result, instead of dry etching we use $0.1\,\%\ \mathrm{H_3PO_4}$ to etch YBCO film after lithography. However one important consequence of the wet etching is its difficulty in time control, hence there is a very poor yield in meandering wire fabrication. With this in mind, we produced a simple bridge with a $2.5\,\mathrm{\mu m}$ width for our first test as shown in Fig. 8.
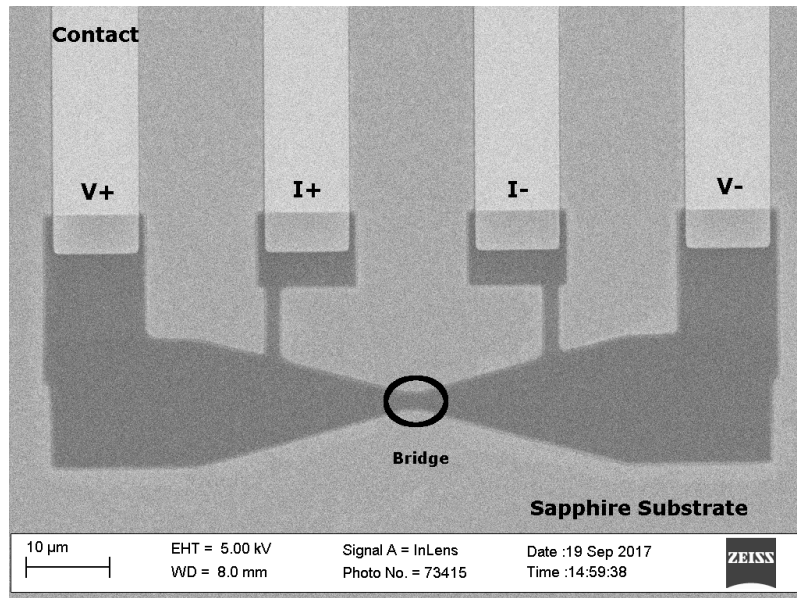

Figure 8: SEM image of the YBCO-bridge. The gold contacts (V_+, V_-, I_+, I_-) for four point measurement are indicated. The bridge is designed to be $2.5\,\mathrm{\mu m}$ wide.

T_c determination with $\frac{R}{2}$-criterion

One of the most important characteristic values of the detector is the critical temperature T_c. To get such values the resistivity as a function of temperature was measured in the PPMS from $77\,\mathrm{K}$ to $300\,\mathrm{K}$, as shown in Fig. 9. The resistivity jump at $100\,\mathrm{K}$ is due to a change of the measuring range from the PPMS and has no physical meaning. For T_c determination from a resistivity measurement, we used the $\frac{R}{2}$-criterion [31]. Using such a criterion the measured data are fitted with two linear functions, one above the transition and one within

the transition (inset Fig. 9). The value of R is determined by the intersection of those two lines. As a result, T_c is the temperature where the resistivity has only half of this value R, and we got a critical temperature T_c of 84 K for this sample.
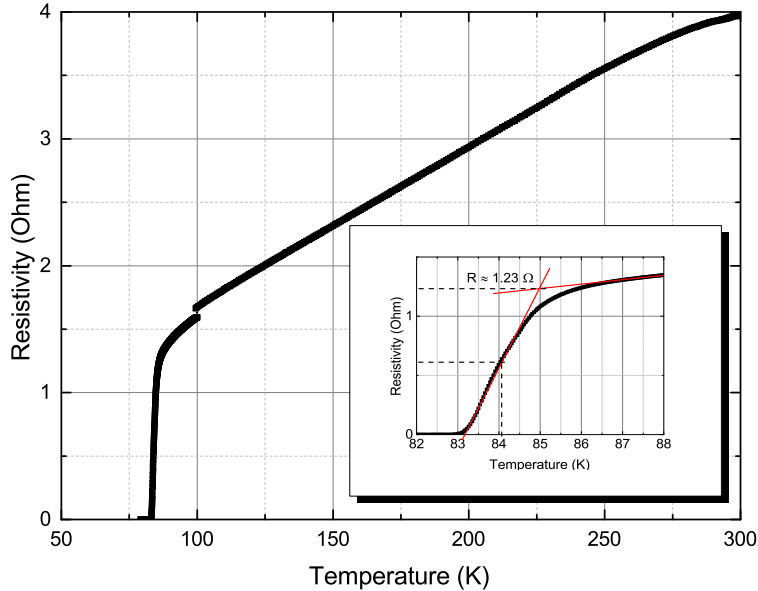

Figure 9: Resistivity measurement of the 150 nm thick, nominal 2.5 µm wide YBCO-bridge performed in the PPMS. The resistivity jump at 100 K is due to a change of the measuring range from the PPMS and has no physical meaning. The critical temperature T_c is 84.1 K by using the $\frac{R}{2}$ criterion (see inset).

Ginzburg-Landau fit of $I_c(T)$

In the next step we measured the bridge's critical current I_c at different operation temperatures in PPMS. Fig. 10 shows the measured I-V curves in a temperature range from 40 K to 80 K. The highest value of the current is used as I_c. The cut-off at 21 V is due to voltage limitation of the current source (Keithley 2400). The finite slope at low voltages is due to contact resistance and the two point measurement. At lower temperatures (below 65 K) a sharp transition from normal to superconducting state was measured, while as the temperature increases the transition becomes blurry. The shape of the IV curve is caused by dissipative movement of magnetic vortices [8].

The critical current I_c at each temperature is plotted in Fig. 11. One error data point was removed. It is important to note that the I_c measurement on the PPMS is not that easy due to several technical problems during the measurement. First of all, the measurement module in PPMS did not perform perfectly for the high values of I_c, namely up to 80 mA in the case of 150 nm thick and 2.5 µm wide bridge. A sharp transition from superconducting to normal state tends to produce high Joule heat, leading to damage of the bridge. The two

17

factors above cause a low reproducibility and large error bars on the I_c data.

In order to describe the temperature dependence of the critical current, we use Ginzburg-Landau (GL) theory to fit the data [32]. In GL-theory the critical current can be described with the following expression

$$I_c = I_c(0) \cdot \left(1 - \frac{T}{T_c}\right)^{\frac{3}{2}} , \qquad (4)$$

where T_c is the critical temperature, and $I_c(0)$ is the critical current at $0\,\mathrm{K}$ and it is an adjustable parameter in the fitting. With $\chi^2_{red} > 0.99$ the data agrees quantitatively well with the GL-theory. We obtained the parameters $I_c(0) = 232.5\,\mathrm{mA}$ and $T_c = 81.3\,\mathrm{K}$, and the latter one agrees with the measured T_c as shown in Fig. 9.
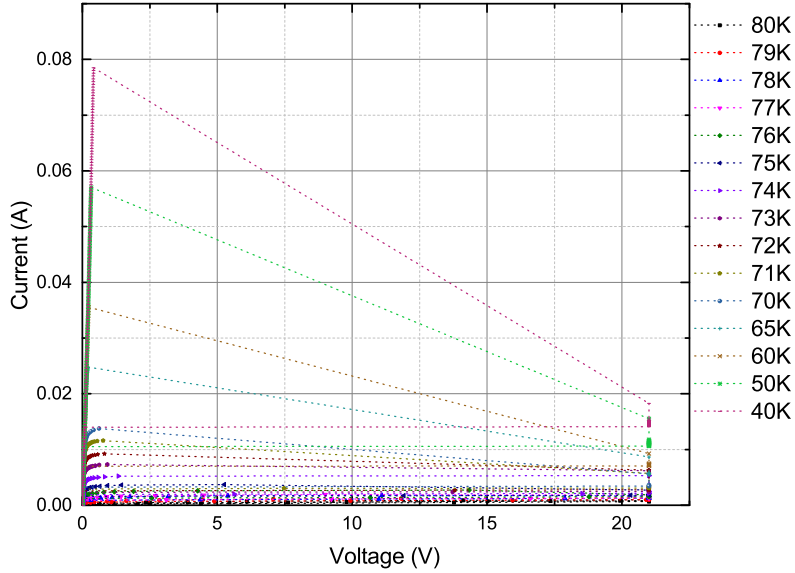
Figure 10: I-V curves of the $150\,\mathrm{nm}$ thick YBCO bridge performed in the PPMS from $40\,\mathrm{K}$ to $80\,\mathrm{K}$. At lower temperatures (below $65\,\mathrm{K}$) a sharp transition from normal to superconducting state was measured. The cut-off at $21\,\mathrm{V}$ is due to voltage limitation of the Keithley 2400 current source.

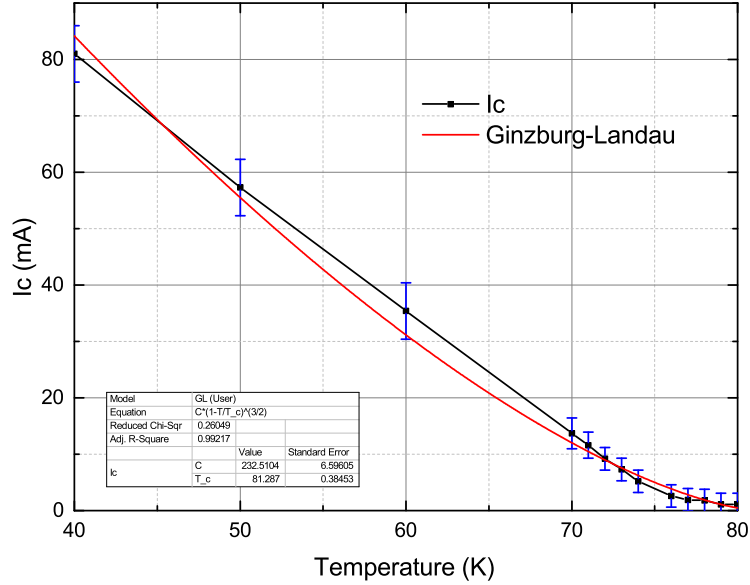| Model	GL (User)	
Equation	C*(1-T/T_c)^(3/2)	
Reduced Chi-Sqr	0.26049	
Adj. R-Square	0.99217	
		Value	Standard Error
Ic	C	232.5104	6.59605
	T_c	81.287	0.38453

Figure 11: I_c as a function of temperature for the 150 nm thick YBCO bridge measured in the PPMS. The $I_c(T)$ can be described by GL theory.

In order to investigate the bridge's response to the X-ray, we transfer the sample to the Cryostat, which couples the Source 1 X-ray source to the sample chamber. As a cross check of I_c measurement in PPMS, we measured the I-V curve in the cryostat at two different temperatures shown in Fig. 12. At 76 K instead of a characteristic transition, one can only see a non-linear increase of the resistance, and at 72 K a characteristic transition is visible at the critical current I_c of 5.2 mA, which is consistent with the result from PPMS measurement. The slope (equals resistance shown in inset Fig. 12) after transition is more than an order of magnitude higher than the finite slope at small voltages, where the finite slope corresponds to the small resistance of the circuit due to the 2 point measurement and the contact resistance.
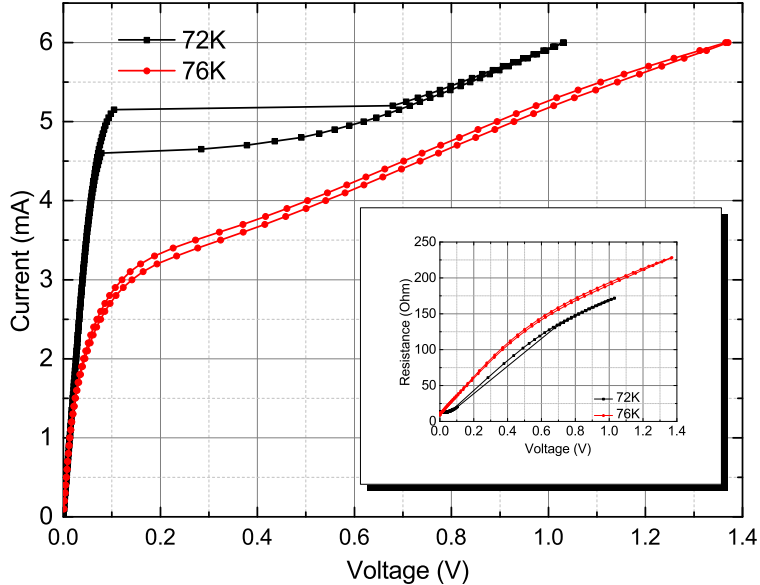
19

Figure 12: I-V curve of the 150 nm thick and 2.5 μm wide YBCO bridge performed in the cryostat at two different temperatures. Only at 72 K are the expected hysteretic effect and the characteristic transition at I_c visible. The finite slope at small voltages is due to the circuit resistance. Inset: Resistance vs. Voltage calculated from the I-V curve. Similarly, only at 72 K is a clear hysteretic behaviour seen.

Pulse shape analysis

For X-ray detection measurement, we operated the YBCO-bridge with 99 % I_c at 72 K in the irradiation with a quite high photon flux (new X-Ray source, 30 keV and 1.5 mA), after 20 min integration only 2 events have been detected (see Fig. 13). The shape of the two events is comparable, so it is obvious that they have the same physical origin. The expected shape came from the equivalent circuit shown Fig. 14, where the (X-)SNSPD is treated as an inductance and a resistor shorted by a switch (e.g. the physical process that the wire becomes normal corresponds to the opening of the switch). The original pulse is produced across the bridge when the bias current shunts to the RF branch of the Bias-Tee due to the switch-open after the bridge becomes resistive from superconducting, and after a 68.4 dB amplification it is collected by an Oscilloscope (Tektronix 7300). The following overshoots after the main peak are reflections of the signal because of the impedance mismatch of the circuit, while a regular signal of a detection event in a circuit with matched impedance is shown in Fig. 15, [30], using a similar circuit. The deformed signal from the bridge is from the circuit design, which needs to be improved in the next step. Nevertheless there are two arguments that the signals are not photon detection events:

- We fitted the first peak's rising and falling edge with two exponential functions

20

$$A_r = A_{r0} + A_{r1} \exp^{\left(\frac{t}{\tau_{rising}}\right)} \tag{5}$$

$$A_f = A_{f0} + A_{f1} \exp^{\left(\frac{t}{\tau_{rising}}\right)}, \tag{6}$$

where A_{r0}, A_{r1}, A_{f0}, A_{f0}, τ_{rising} and $\tau_{falling}$ are fitting parameters. We got two time constants $\tau_{rising} \approx 28\,\text{ns}$ and $\tau_{falling} \approx 43\,\text{ns}$. Due to the equivalent circuit (Fig. 14) one can calculate the kinetic inductance L_k and the resistance of the bridge in normal state R_n with the following expressions:

$$\tau_{rising} = \frac{L_k}{R_n + R_L} \tag{7}$$

$$\tau_{falling} = \frac{L_k}{R_L}, \tag{8}$$

where $R_L = 50\,\Omega$ is the impedance of the RF circuit [16]. $R_n = 27\,\Omega$ and the calculated kinetic inductance of about $220\,\text{nH}$ does not fit the experimental setup with a $300\,\text{nH}$ inductor in series with the detector.

- With the voltage amplitude of the pulse, one can calculate the amount of current that goes to the readout circuit. The amplitude of the voltage pulse after ($g = 68.4\,\text{dB}$) amplification $V_{ampl} = 0.4\,\text{V}$. This means that the original amplitude

$$V_{ampl.} = V_{orig.} \cdot g \Rightarrow V_{orig.} = \frac{V_{ampl.}}{g} = \frac{0.4\,\text{V}}{10^{\frac{68.4}{20}}} = 0.15\,\text{mV}. \tag{9}$$

  With the readout impedance one can calculate the current that goes to the readout

$$I_b' = \frac{V_{orig.}}{R_L} = \frac{0.15\,\text{mV}}{50\,\Omega} \approx 3\,\text{μA}. \tag{10}$$

.

  The bias current is $5\,\text{mA}$ so only $0.6\,\%$ of the current goes to the readout, namely the detector is not fully in normal state.

Taking into account all arguments above we think that these pulses are not photon detection events. The two pulses seem to be caused by thermal fluctuations in the bridge. Since the relative temperature $\frac{T}{T_c} = \frac{72\,\text{K}}{84\,\text{K}} = 86\,\%$ and bias current ratio $\frac{I_b}{I_c} = 99\,\%$ is high, at such combination dark count event (by thermal fluctuations) can happen [18]. We attribute the failure of the X-SNSPDs photon detection to the large dimension of the bridge, i.e. including both width ($2.5\,\text{μm}$) and thickness ($150\,\text{nm}$). We then tried a $200\,\text{nm}$ wide bridge (Fig. 16) but no transition IV curve for single photon response was observed. We think that the thickness dominates the sensitivity of the detector. This argument is also supported by a recent experiment, that a single photon detection has

been observed by an optical SNSPD with a thickness of 5 μm and a large width of 2.12 μm [33]. Based on this idea we decide to decrease the thickness of the 150 nm thick film. Two advantages are expected:

1. The sensitivity could be improved for single X-ray detection

2. Narrower bridges/wires can be more easily fabricated due to the lower thickness-width ratio.
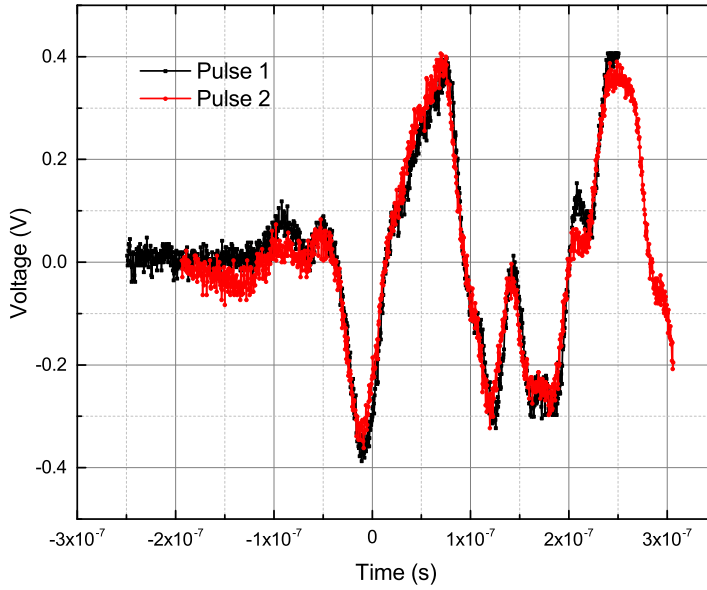

Figure 13: Two measured pulses during irradiation of the bridge with the new X-ray tube with an integration time of ≈ 20 min. The original pulse is produced across the bridge and then shunts to the RF branch of the Bias-Tee, and after a 68.4 dB amplification it is collected by an Oscilloscope (Tektronix 7300). The following overshoots are caused by the impedance mismatch of the whole circuit. The two pulses seems to be caused by thermal fluctuations in the bridge (see main text for a more detailed discussion).
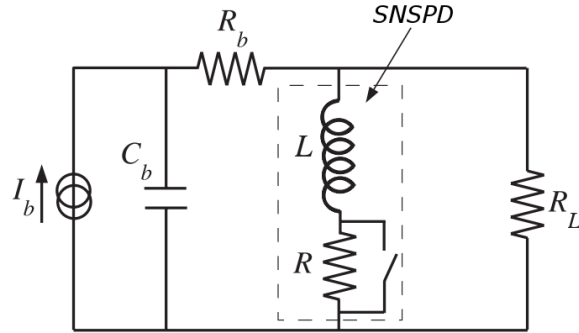
Figure 14: SNSPD equivalent circuit of standard single-wire SNSPD [16]. In our case the resistance $R_L = 50\,\Omega$.
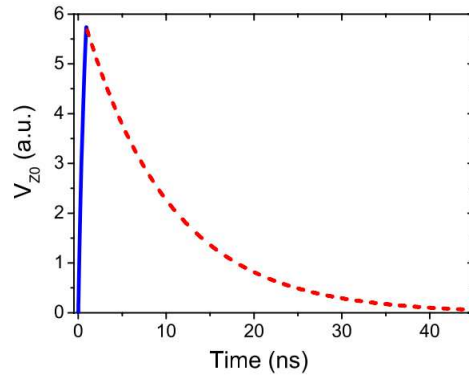

Figure 15: A simulation of the output voltage pulse of the SNSPD [17]. The sign depends on the number of used amplifiers. A more detailed discussion is given in Ref. [34].
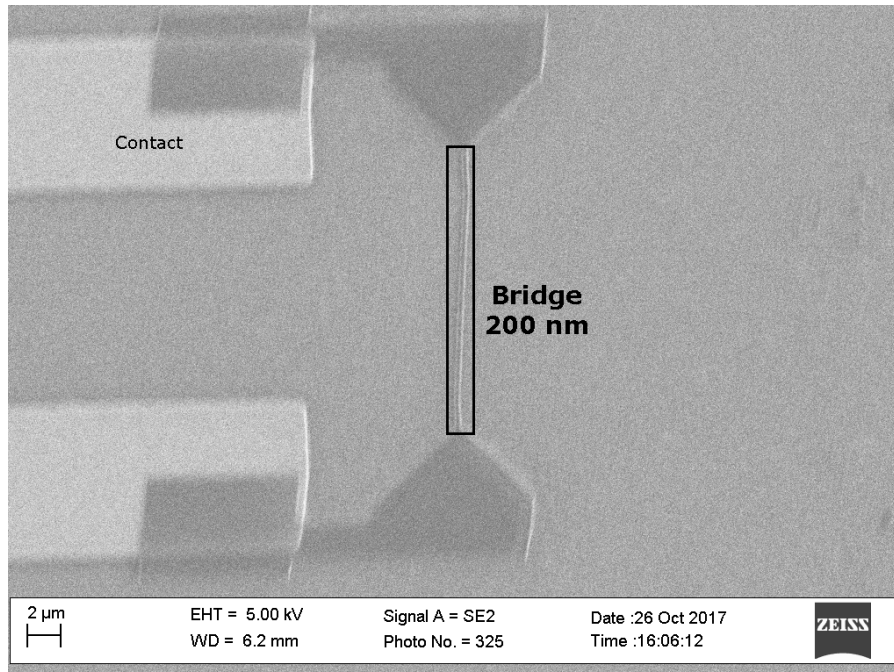
Figure 16: SEM image of a YBCO bridge made out of a 150 nm film. The deformation of the image is due to the bad contact between sapphire substrate and the sample holder of SEM.

3.2 Reduced 150 nm thick YBCO-films

Due to the unsuccessful measurements for X-ray detection with the 150 nm thick bridge we reduced the thickness of the film from 150 nm down to 70 nm via wet etching with the 0.1 % H_3PO_4 at room temperature in order to fabricate thinner and narrower bridges.

We first measured four 70 nm thick films in PPMS, indexed as Etching 1-4 shown in Fig. 17. It is shown that the T_c of 70 nm after etching has not been decreased with respect to the original 150 nm film. However, the variation of T_c for the four 70 nm etched films indicates the hardly-controlled wet etching.

The 70 nm films are then fabricated into bridges with width of 200 nm. The T_c of the two bridges are measured as well in PPMS, as shown in Fig. 18. The T_c of two bridges degrades to 80 K, and this is caused by a following wet etching after lithography.

We measured the I-V curve of the bridge 1 in the Cryostat at two different temperatures (see Fig. 18). At both temperatures (76 K and 72 K) no characteristic transition is visible, which behaves similarly to the I-V curve at 76 K for the 150 nm thick film. Unfortunately with such a bridge no detection event was recorded.

We characterized the 150 nm and 70 nm thick bridge via SEM as shown in Fig. 16 and 19. It is clear that the surface of the substrate with the 70 nm thick bridge is much rougher than the surface of the substrate with the150 nm thick bridge, since the former sample went through extra wet etching for thickness reduction besides wetting after lithography. The roughness of the substrate is much easier to see, nevertheless we infer that the reduced 70 nm thick bridge degraded more than the 150 nm thick bridge, namely the longer etching also introduces more defects in film quality and bridge geometry, and these water-involved processes lead to a non-transition in I-V curve even at lower temperatures.
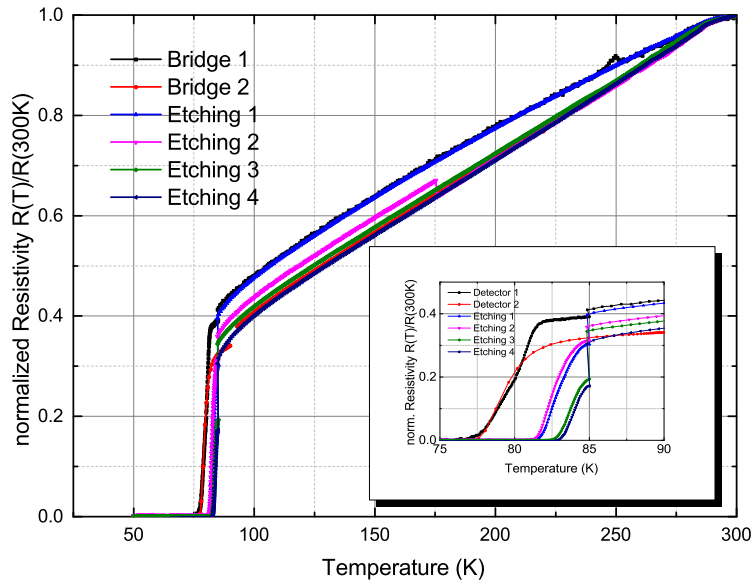
Figure 17: Resistivity measurements of the 150 nm thick YBCO bridge and the etched film performed in the PPMS. Both the bridge and the etched films show a critical temperature T_c of around 80 K.
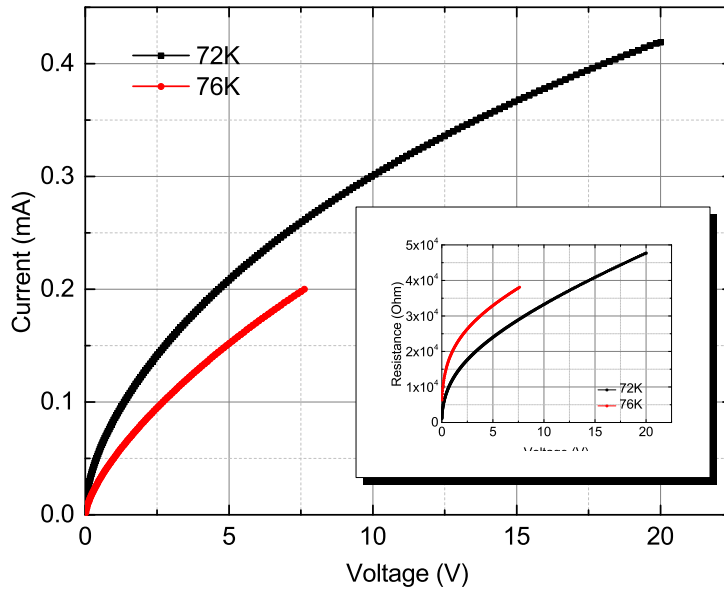

Figure 18: I-V curve of the 70 nm thick YBCO meander (i.e. etched from the 150 nm thick film) performed in the PPMS at different temperatures. At both temperatures no hysteretic effect or characteristic transition at I_c is observed. Inset: Resistance vs. Voltage calculated from the I-V curve. Similarly, at both temperatures no hysteretic behaviour occurs.
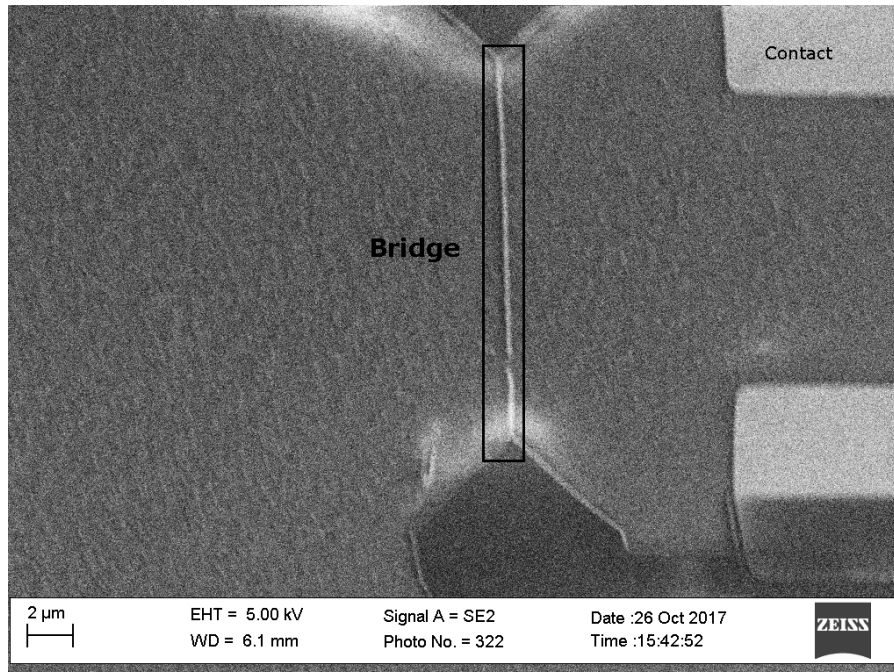
26

Figure 19: SEM image of a $70\,\mathrm{nm}$ thick YBCO bridge. The surface is much rougher than that before etching.

3.3 Thinner films (40 nm and 20 nm) and degradation

Since the 150 nm thick films fail to respond to X-ray photons, and the thinner film (70 nm) obtained from etching the 150 nm film shows no sharp transition in I-V curve due to the etching, we turn to a commercial 40 nm and 20 nm thick film (Ceraco). The thick 150 nm films show a robust $T_c \approx 83\,K$ before and after processing, while the thinner films (20 nm and 40 nm thick) can be more vulnerable to the processing, so we tried to find different parameters that influence the degradation [35, 36]. In our processing water flushing and baking (for lithography and gold contact deposit) are two important issues that can degrade the films.

For the 40 nm films, we baked one of them for 10 min at 75 °C (the same condition for photoresist baking). This baking reduced the critical temperature T_c to 66 K, and the whole temperature dependence including the normal state resistance and the transition width was changed from typical YBCO $R(T)$ behaviour, as shown in Fig. 20.

We then treated another 40 nm film via water flushing. As shown in Fig. 21 the process including flushing with water reduced the critical temperature to 75 K and destroyed the expected shape of the resistivity curve. The resistivity is normalized for better comparability. We did not go further with this 40 nm sample due to its heavily degraded film.
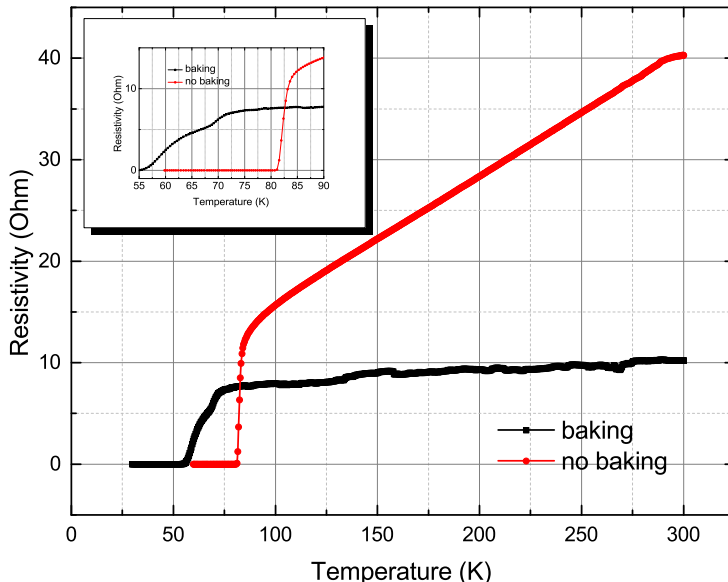

Figure 20: Resistivity measurements of the 40 nm thick YBCO film performed in the PPMS. The critical temperature T_c of the film before baking is 82 K. After baking 10 min at 75 °C, T_c becomes 66 K, indicating the superconductivity degradation caused by baking.
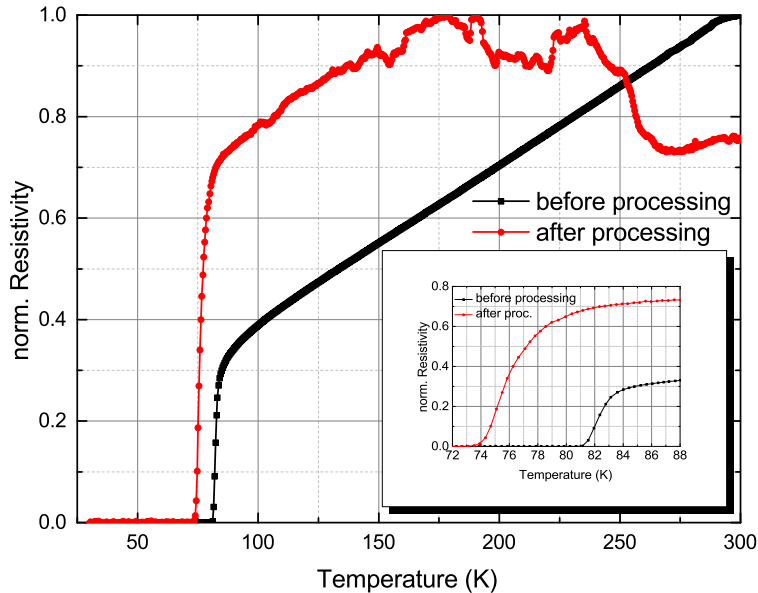
Figure 21: Resistivity measurements of the 40 nm thick YBCO film performed in the PPMS. The critical temperature T_c of the film before processing is 82 K. After processing including flushing with water T_c becomes 75 K, indicating the superconductivity degradation caused by water. The resistivity is normalized for better comparison.

For the 20 nm YBCO films, we directly performed nano fabrication, during which unnecessary flushing and baking process were skipped. Nevertheless, non functional meander structure (100 nm-200 nm wide typically) were fabricated (as shown in Fig. 22), therefore we used again a simple bridge structure (Fig. 23) with nominal width of 200 nm.

The resistivity was measured in the PPMS from 40 K to 300 K, and the measured critical temperature T_c is 72.6 K (Fig. 24) which is much lower than expected.

We conclude that both 40 nm and 20 nm thick films are too thin to fabricate with keeping the quality of the film unchanged. For all the films discussed above with a degraded T_c, we treat them with annealing (400 °C, O_2 atmosphere, 12 h) in order to compensate oxygen loss, however the annealing does not improve T_c at all. The process of oxygen loss and its effects is described in Ref. [37]. We believe beside oxygen leak during store and nano fabrication, more damage processes occur to the films, especially to the thinner films or nano structures [8].
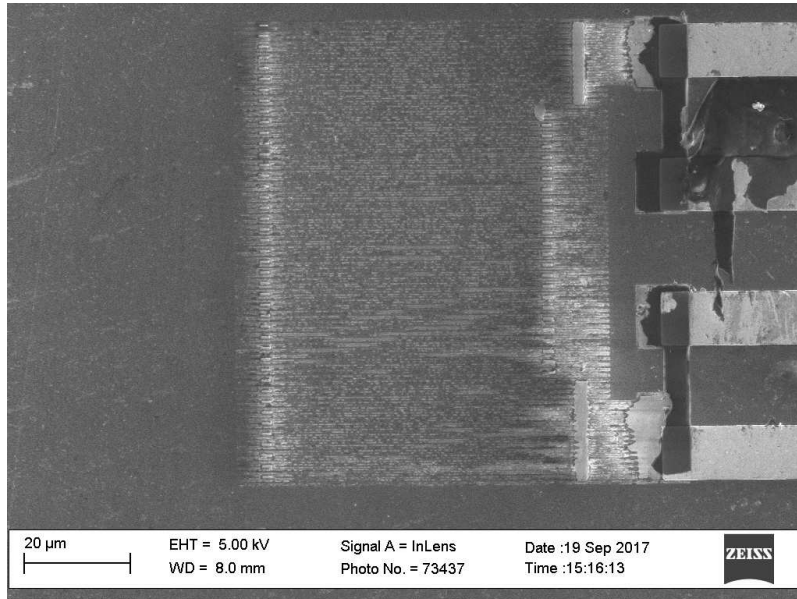
Figure 22: SEM image of the meander produced in 20 nm thick YBCO sample. The meander structure is really bad and there are several interruptions so the detector is neither conducting nor superconducting.
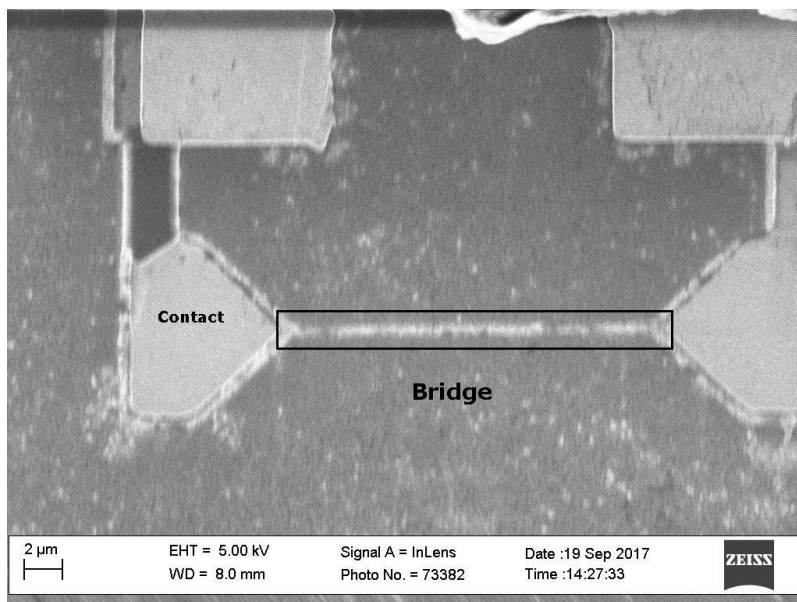

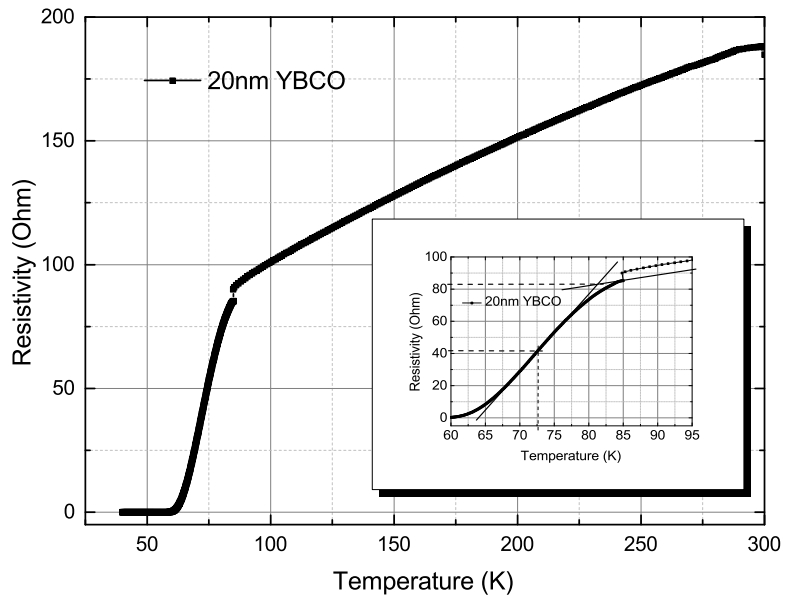Figure 23: SEM image of the 20 nm thick YBCO-bridge used.

Figure 24: Resistivity measurement of the 20 nm thick YBCO bridge performed in the PPMS. The critical temperature T_c is 72.6 K by using the $\frac{R}{2}$ criterion (see inset).

3.4 BSCCO film and bridge

Based on the experience of YBCO, we change our focus on an alternative material. We made measurements with a 300 nm thick BSCCO film (provided by Prof. Akiyoshi Matsumoto, National Institute for Material Science, Japan). The first measurement was a resistivity measurement in the PPMS. The T_c was determined to 115 K according to $\frac{R}{2}$ criterion.
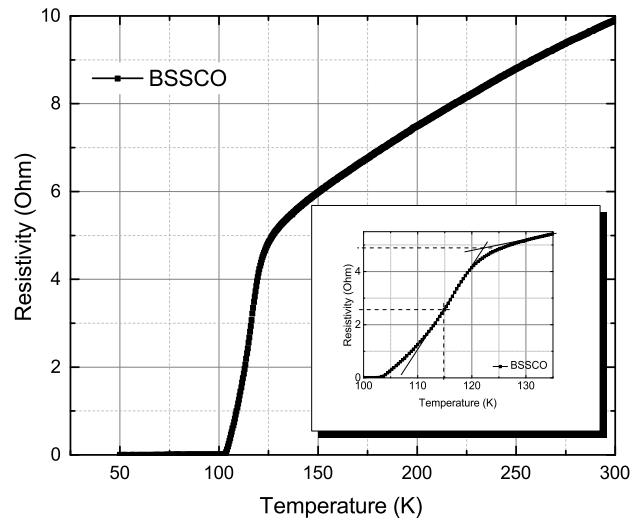

Figure 25: Resistivity measurement of the 300 nm thick BSCCO film performed in the PPMS. The critical temperature T_c is 115 K by using the $\frac{R}{2}$ criterion (see inset).

In order to determine the I_c and the I-V behaviour of the BSCCO film, we fabricated the films into a 100 μm wide bridge. During the fabrication an RIE (Ar environment, 300 W, 100 mTorr, 20 sccm, 600 s) process was used to etch the unwanted BSCCO film. After the fabrication the critical temperature was reduced to 61 K due to the oxygen loss. But afte annealing (400 °C, 10 h, O_2 environment), the critical temperature came back to 106 K (Fig.26). Thus we were able to show that the processing still reduces the critical temperature but it can be compensated by annealing.
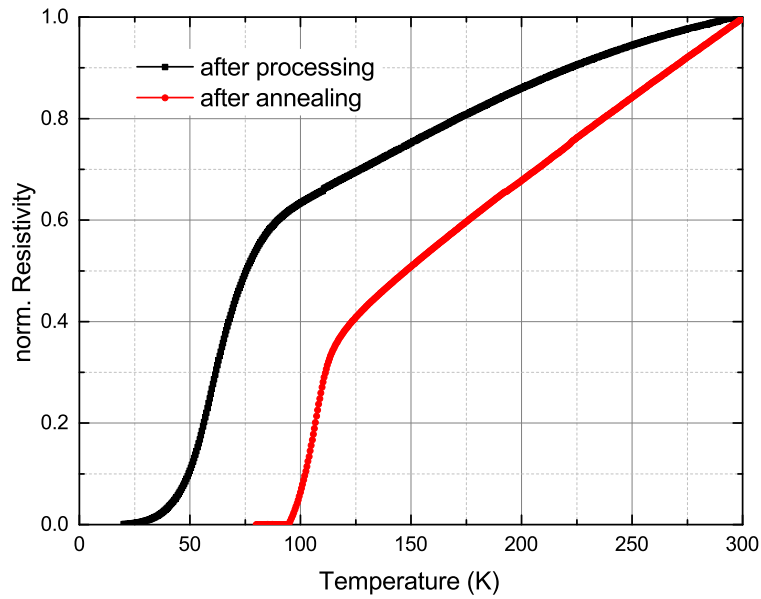
Figure 26: Resistivity measurement of the 300 nm thick BSCCO film perfor-
med in the PPMS. The black and the red curves show the measurement after
processing and after annealing respectively. The critical temperatures are 61 K
after processing and 106 K after annealing. The resistivity is normalized for
better comparability.

In the next step, we are going to reduce the thickness of the BSCCO (via
RIE) and make narrower wires. With smaller dimensions we expect to see a
transition- included IV curve and single photon response.

4   Conclusions and Outlook

The first measurements were done with the 150 nm thick YBCO film. Due to the ceramic properties of YBCO it is difficult to etch the YBCO film via RIE, so we used wet etching. Moreover considering the poor yield in meander fabrication we focused on a simple bridge structure. We characterized the film in the PPMS, and determined a critical temperature of 84.1 K with the $\frac{R}{2}$ criterion. We then measured the bridge's critical current I_c at different temperatures in PPMS and applied with Ginzburg-Landau theory to the resulting data. The data agrees quantitatively well with theory ($\chi^2_{red} > 0.99$) and the fitting parameters ($I_c(0) = 228$ mA and $T_c = 81.9$ K) are consistent with the measurements.

After mechanical adjustments at the cryostat we installed a new X-ray source (Source 1 X-Ray). We measured the emission spectrum with a Si-PIN X-ray photon counter and compared it with the emission spectrum of the old Oxford tube. Despite the non-ideal spectrum for the new X-ray tube, the total amount of emitted photons per second is comparable to the old tube with the same settings of driven voltage and current.

In order to investigate the bridge's response to the X-ray, we transferred the sample to the Cryostat. As a cross check of I_c measurement in PPMS, we measured the I-V curve in the cryostat at two different temperatures. Only at 72 K is a characteristic transition visible with the critical current I_c of 5.2 mA.

For X-ray detection measurement, we operated the YBCO-bridge with 99 % I_c at 72 K in the irradiation with a quite high photon flux. After 20 min integration only two events have been detected, which can originate from thermal fluctuations in the bridge.

We then tried the etched 150 nm (i.e. 70 nm), 40 nm and 20 nm films, but they degraded too much to get a good I-V behaviour or T_c.

We conclude that for thick films the detector is not sensitive enough and thin films are too thin to fabricate, in order to maintain good quality of the films. Finally we tried the 300 nm thick BSCCO film. The critical temperature was 115 K. After nano fabrication (via RIE) an annealing process can fix the drop of the critical temperature to 61 K and bring the critical temperature back to 106 K.

As a next step in this project, we will fabricate thinner and narrower BSCCO bridges/meander, in order to observe X-ray single photon response in X-SNSPDs. Another important focus is the understanding of the process of the X-ray photon detection.

5   Acknowledgements

I would like to thank Prof. Dr. A. Schilling for giving me the opportunity to do my Master Thesis on this interesting project. I would also like to thank Dr. Qiang Wang and Dr. Zhang for welcoming me to the group and most of all for their continuous support, help and advice during the entire period of this thesis.

References

[1] H. Kamerlingh Onnes. *Proceedings*, 13(II):1274, 1911. Also published as: Communications of the Physical Laboratory of the University of Leiden, no 120b.

[2] M. Tinkham. *Introduction to Superconductivity.* Dover Publications, Inc., New York, 1996. 2nd ed.

[3] D. van Delft and P. Kes. The discovery of superconductivity. *Physics Today*, 63(9):38–43, 2010. `doi:10.1063/1.3490499`.

[4] Supraleitung, Gruppe A. Schilling UZH. `http://www.physik.uzh.ch/groups/schilling/supra.html`. Accessed: 2018-02-17.

[5] J. Bardeen, L. N. Cooper, and J. R. Schrieffer. Theory of Superconductivity. *Phys. Rev.*, 108(5):1175–1204, 1957. `doi:10.1103/PhysRev.108.1175`.

[6] M. K. Wu, J. R. Ashburn, C. J. Torng, P. H. Hor, R. L. Meng, L. Gao, Z. J. Huang, Y.Q. Wang, and C. W. Chu. Superconductivity at 93 K in a new mixed-phase Y-Ba-Cu-O compound system at ambient pressure. *Phys. Rev. Letters*, 58(9):908–910, 1987. `doi:10.1103/PhysRevLett.58.908`.

[7] E. Stilp, A. Suter, T. Prokscha, Z. Salman, E. Morenzoni, H. Keller, P. Pahlke, Hühne R., C. Bernhard, R. Liang, W. N. Hardy, D. A. Bonn, J. C. Baglo, and R. F. Kiefl. Controlling the near-surface superfluid density in underdoped $YBa_2Cu_3O_{6+x}$ by photo-illumination. *Scientific Reports*, 4(6250), 2014. `doi:10.1038/srep06250`.

[8] P. Thoma. *Ultra-fast $YBa_2Cu_3O_{7-x}$ direct detectors for the THz frequency range.* KIT Scientific Publishing, Karlsruhe, 2013. Band 009.

[9] Shaikh Md. Rubayiat Tousif and Shaiyek Md. Buland Taslim. Preparation, Verification and Finding Out of the Critical Current of Thin Sample of YBCO Compounds. *IJSER*, 2(3), 2011.

[10] S. E. Russek, S. C. Sanders, A. Roshko, and J. W. Ekin. Surface degradation of superconducting $YBa_2Cu_3O_{7-d}$ thin films. *Appl. Phys. Lett.*, 64(26), 1994.

[11] H. Maeda, Y. Tanaka, M. Fukutomi, and T. Asano. A new high-Tc oxide superconductor without a rare earth element. *Japanese Journal of Applied Physics*, 27(2):L209–L210, 1988.

[12] D. A. Cardwell and D. S. Ginley. *Handbook of Superconducting Materials, Volume 1: Superconductivity, Materials and Process.* Institute of Physics Publishing, Bristol and Philadelphia, 2003. C2 BSCCO by P.N. Mikheenko, K. K. Uprety and S. X. Dou.

[13] L. R. Testardi. Destruction of Superconductivity by Laser Light. *Phys. Rev. B*, 4(7):2189–96, 1971. `doi:10.1103/PhysRevB.4.2189`.

[14] P. L. Richards. Bolometers for infrared an millimeter waves. *J. Appl. Phys.*, 76(1):1–24, 1994. `doi:10.1063/1.357128`.

[15] G. N. Gol'tsman, O. Okunev, G. Chulkova, A. Lipatov, A. Semenov, K. Smirnov, B. Voronov, A. Dzardanov, C. Williams, and Roman Sobolewski. Picosecond superconducting single-photon optical detector. *Appl. Phys. Lett.*, 79(6):705–7, 2001. `doi:10.1063/1.1388868`.

[16] G. Goltsman, A. Korneev, A .Divochiy, O. Minaeva, M. Tarkhov, N. Kaurova, V. Seleznev, B. Voronov, O. Okunev, A. Antipov, K. Smirnov, Yu. Vachtomin, I. Milostnaya, and G. Chulkova. Ultrafast superconducting single-photon detector. *Journal of Modern Optics*, 56(15), 2009. `doi:10.1080/09500340903277750`.

[17] C. M. Natarajan, M. G. Tanner, and R. H. Hadfield. Superconducting nanowire single-photon detectors: physics and applications. *Supercond. Sci. Technol.*, 25(6):1–16, 2012. `doi:10.1088/0953-2048/25/6/063001`.

[18] A. Engel, J. J. Renema, K. Il'in, and A. Semenov. Detection mechanism of superconducting nanowire single-photon detectors. *Supercond. Sci. Technol.*, 28(11):1–22, 2015. `doi:10.1088/0953-2048/28/11/114003`.

[19] J. J. Renema, R. Gaudio, Q. Wang, Z. Zhou, A. Gaggero, F. Mattioli, R. Leoni, D. Sahin, M. J. A. de Dood, A. Fiore, and M. P. van Exter. Experimental Test of Theories of the Detection Mechanism in a Nanowire Superconducting Single Photon Detector. *Phys. Rev. Lett.*, 112(11), 2014. `doi:10.1103/PhysRevLett.112.117604`.

[20] H. N. Chapman, A. Barty, M. J. Bogan, S. Boutet, M. Frank, S. P. Hau-Riege, S. Marchesini, B.W. Woods, S. Bajt, W. H. Benner, R. A. London, A. Plönjes, M. Kuhlmann, R. Treusch, S. Düsterer, T. Tschentscher, J. R. Schneider, E. Spiller, T. Möller, Ch. Bostedt, M. Hoener, D. A. Shapiro, K. O. Hodgson, D. van der Spoel, F. Burmeister, M. Bergh, C. Caleman, G. Huldt, M. M. Seibert, F. N. C. Maia, R. W. Lee, A. Szöke, N. Timneanu, and J. Hajdu. Femtosecond diffractive imaging with a soft-X-ray free-electron laser. *Nature Physics*, 2:839–843, 2006. `doi:10.1038/nphys461`.

[21] F. Marsili, V. B. Verma, J. A. Stern, S. Harrington, A. E. Lita, T. Gerrits, I. Vayshenker, B. Baek, M. D. Shaw, R. P. Mirin, and S. W. Nam. Detecting single infrared photon with 93% system efficiency. *Nature Photonics*, 7:210–214, 2013. `doi:10.1038/nphoton.2013.13`.

[22] L. You, X. Yang, Y. He, W. Zhang, D. Liu, W. Zhang, L. Zhang, X. Liu, S. Chen, Z. Wang, and X. Xie. Jitter analysis of a superconducting nanowire single photon detector. *AIP Advances*, 3(7):1–6, 2013. `doi:10.1063/1.4817581`.

[23] M. S. Allman, V. B. Verma, M. Stevens, T. Gerrits, R. D. Horansky, A. E. Lita, F. Marsili, A. Beyer, M. D. Shaw, D. Kumor, R. Mirin, and S. W. Nam. A near-infrared 64-pixle superconducting nanowire single photon

detector array with integrated multiplexed readout. *Appl. Phys. Lett.*, 106(19):1–4, 2015. `doi:10.1063/1.4921318`.

[24] A.E. Lita, V.B. Verma, R. D. Horansky, J.M. Shainline, R.P. Mirin, and S. Nam. Materials Development for High Efficiency Superconducting Nanowire Single-Photon Detectors. *MRS Proceedings*, 1807:1–6, 2015. `doi:10.1557/opl.2015.544`.

[25] H. Shibata, T. Akazaki, and Y. Tokura. Fabrication of MgB_2 Nanowire Single-Photon Detector with Meander Structure. *Applied Physics Express*, 6(2):1–3, 2013. `doi:10.7567/APEX.6.023101`.

[26] X. Zhang, Q. Wang, and A. Schilling. Superconducting single X-ray photon detector based on $W_{0.8}Si_{0.2}$. *AIP Advances*, 6(11):1–5, 2016. `doi:10.1063/1.4967278`.

[27] K. Inderbitzin, A. Engel, K. Il'in, and M. Siegel. An ultra-fast supercon-duction Nb nanowire single-photon detector for soft x-rays. *Appl. Phys. Lett.*, 101(16):1–5, 2012. `doi:10.1063/1.4759046`.

[28] K. Inderbitzin, A. Engel, and A. Schilling. Soft X-Ray Single Photon De-tection With Superconducting Tantalum Nitride and Niobium Nanowires. *IEEE*, 23(3):1–5, 2013. `doi:10.1109/TASC.2012.2234496`.

[29] N. Curtz, E. Koller, H. Zbinden, M. Decroux, L. Antagnazza, O. Fis-cher, and N. Gisin. Patterning of ultrathin YBCO nanowires using a new focused-ion-beam process. *Supercond. Sci. Techn.*, 25(4):1–6, 2010. `doi:10.1088/0953-2048/23/4/045015`.

[30] Adrian Aeschbacher. Superconducting Nanowire Single-Photon Detectors based on TaN Thin Films. Master Thesis, Universität Zürich, 2011.

[31] C. Barth. *High Temperature Superconductor Cable Concepts for Fusion Magnets.* Scientific Publishing, Karlsruhe, 2013. p. 8.

[32] M. Ohmukai, T. Fujita, and Takayuki Ohno. The temperature dependence of critical current in $YBa_2Cu_3O_{7-d}$ thin films deposited on MgO by an eclipse PLD. *Brazilian Journal of Physics*, 31(3), 2001. `doi:10.1590/S0103-97332001000300027`.

[33] Y. Korneeva, D. Yu. Voalazov, Semenov A. V, I. Florya, N. Simonov, E. Ba-eva, A. A. Korneev, G. N. Goltasman, and T. M. Klapwijk. Optical single photon detection in micron-scaled NbN bridges. *eprint arXiv:1802.02881*, 2018. URL: `https://arxiv.org/abs/1802.02881`.

[34] J. K. W. Yang, A. J. Kerman, E. A. Dauler, V. Anant, K. M. Rosfjord, and K. K. Berggren. Modeling the Eletrical and Thermal Response of Superconducting Nanowire Singel-Photon Detectors. *IEEE*, 17(2):581–585, 2007. `doi:10.1109/TASC.2007.898660`.

[35] R. Arpaia, D. Golubev, R. Baghdadi, R. Ciancia, G. Drazic, P. Orgiani, D. Montemurro, T. Bauch, and F. Lombardi. Transport properties of ultrathin $YBa_2Cu_3O_{7-d}$ nanowires: A route to single photon detection. *Phys. Rev. B*, 96(6), 2017. `doi:10.1103/PhysRevB.96.064525`.

[36] R. Arpaia, M. Ejrnaes, L. Parlato, R. Cristiano, M. Arzeo, T. Bauch, S. Nawaz, F. Tafuri, G. P. Pepe, and F. Lombardi. Highly homogeneous YBCO/LSMO nanowires for photoresponse experiments. *Superconductor Science and Technology*, 27(4), 2014. `doi:10.1088/0953-2048/27/4/044027`.

[37] Dong Han Ha, H. S. Min, Kang-Won Lee, S Byon, G. Y. Han, and H. K. Lee. Effects of cation substitution on the oxygen loss in YBCO superconductors. *Journal of the Korean Physical Society*, 39(6):1041–1045, 2001.